J. Fluid Mech. (2019), *vol.* 866, *pp.* 298–315.
doi:10.1017/jfm.2019.117

A theory on the spreading of impacting droplets

José Manuel Gordillo[1],†, Guillaume Riboux[1] and Enrique S. Quintero[1]

[1]Área de Mecánica de Fluidos, Departamento de Ingenería Aeroespacial y Mecánica de Fluidos, Universidad de Sevilla, Avenida de los Descubrimientos s/n 41092, Sevilla, Spain

(Received 5 November 2018; revised 15 January 2019; accepted 1 February 2019; first published online 5 March 2019)

Here we provide a self-consistent analytical solution describing the unsteady flow in the slender thin film which is expelled radially outwards when a drop hits a dry solid wall. Thanks to the fact that the fluxes of mass and momentum entering into the toroidal rim bordering the expanding liquid sheet are calculated analytically, we show here that our theoretical results closely follow the measured time-varying position of the rim with independence of the wetting properties of the substrate. The particularization of the equations describing the rim dynamics at the instant the drop reaches its maximal extension which, in analogy with the case of Savart sheets, is characterized by a value of the local Weber number equal to one, provides an algebraic equation for the maximum spreading radius also in excellent agreement with experiments. The self-consistent theory presented here, which does not make use of energetic arguments to predict the maximum spreading diameter of impacting drops, provides us with the time evolution of the thickness and of the velocity of the rim bordering the expanding sheet. This information is crucial in the calculation of the diameters and of the velocities of the droplets ejected radially outwards for drop impact velocities above the splashing threshold.

Key words: aerosols/atomization, drops

1. Introduction

The precise description of the rich events following the impact of a drop against a dry solid has been the subject of a number of recent contributions, see e.g. Roisman (2009), Eggers *et al.* (2010), Laan *et al.* (2014, 2015), Visser *et al.* (2015), Lee *et al.* (2016), Wildeman *et al.* (2016), Wang & Bourouiba (2017), Wang *et al.* (2018) for its profound implications in countless applications like printing, the modelling of spray coating or the prediction of the spreading of contaminants by rain drops between neighbouring leaves (Josserand & Thoroddsen 2016; Lejeune, Gilet & Bourouiba 2018). With only a few exceptions (Roisman, Rioboo & Tropea 2002; Eggers *et al.* 2010; Villermaux & Bossa 2011), most of the published results are limited to reporting the maximum spreading radii of the impacting drops. In these works, the results of the maximum radial extension reached by the falling droplets are expressed in terms of the different dimensionless parameters governing this common physical situation and also as a function of the type of substrate, which can be a hydrophilic

† Email address for correspondence: jgordill@us.es

solid (Roisman 2009; Antonini, Amirfazli & Marengo 2012; Visser *et al.* 2015), a superhydrophobic solid (Clanet *et al.* 2004; Antonini *et al.* 2012; Lv *et al.* 2016; Quintero, Riboux & Gordillo 2019) or a vapour layer, which is the practical way of imposing a stress free boundary condition at the bottom of the expanding drop (Tsai *et al.* 2011; Tran *et al.* 2012).

The present contribution goes beyond the number of studies that focus on the prediction of the maximum spreading radii of impacting droplets: indeed, our theoretical results can also be used to calculate the time evolution of the position of the rim limiting the expanding liquid sheet as well as its thickness. This information is essential to predicting the diameters and velocities of the droplets ejected for drop impact velocities beyond the splashing threshold (Riboux & Gordillo 2015).

The main idea in the present contribution is that we report an analytical solution for the unsteady flow in the thin liquid film region coupling the flow in the impacting drop with that in the toroidal rim bordering the expanding liquid sheet. In this way, we are able to precisely quantify the unsteady fluxes of mass and momentum that are being injected into the rim and, following the ideas in Eggers *et al.* (2010), Villermaux & Bossa (2011), Riboux & Gordillo (2015), we apply mass and momentum balances at the rim to deduce the ordinary differential equations governing the time evolution of the rim radial position and thickness. We validate our theory by comparing our predictions with the experimental data available in the literature and also with our own experimental observations.

In § 2 we describe the experimental set-up and also present the simplified equations describing the flow. Section § 3 is devoted to providing an analytical solution to the equations governing the slender flow region located upstream of the rim, in § 4 the theoretical predictions are compared with experimental measurements and conclusions are presented in § 5.

2. Description of experiments and of the equations governing the flow

Two high speed cameras have been placed perpendicularly to each other to record simultaneously the impact of water drops of radii R falling from rest over a dry solid at a velocity V. With the purpose of analysing the influence of the wetting properties of the solid on the drop spreading dynamics, the substrate can be either a smooth solid surface or a substrate covered by a commercial superhydrophobic coating (Lv *et al.* 2016; Quintero *et al.* 2019). Drops are formed quasi-statically at normal atmospheric conditions and the origin of time, $T = 0$, is set at the instant the drop first touches the solid, see figure 1. The Ohnesorge, Reynolds, Weber and capillary numbers are defined here as $Oh = \mu/\sqrt{\rho R\sigma}$, $Re = \rho VR/\mu$, $We = Oh^2\,Re^2$, $Ca = \mu V/\sigma$ with ρ, μ and σ indicating the liquid density, viscosity and interfacial tension coefficient respectively. Figure 1 illustrates that, while the bottom of the falling droplet always touches the substrate, the edge of the expanding lamella may be or not in contact with the solid. Indeed, for the case of superhydrophobic coatings, the rim never touches the substrate whereas for the case of smooth hydrophilic or hydrophobic substrates the rim will take-off from the solid only when the aerodynamic lift is strong enough (Riboux & Gordillo 2014).

Before presenting the equations governing the rim dynamics and the flow in the so-called lamella region, which is located upstream the rim, see figure 1, let us point out first that we will follow the notation in Riboux & Gordillo (2014) and, in the text, dimensionless variables will be written using lower case letters to differentiate them from their dimensional counterparts (in capital letters). In addition, distances, times

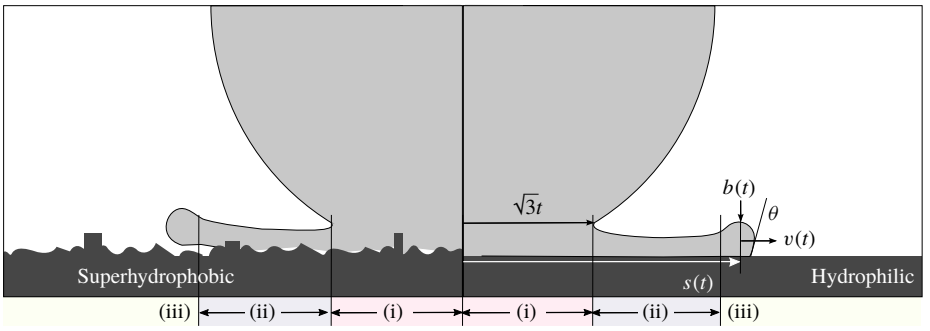

FIGURE 1. (Colour online) Sketch showing a drop spreading along a substrate which can be covered or not with a superhydrophobic material, represented here with a rough texture. The experiments to be presented next will be conducted by impacting drops against either smooth hydrophilic substrates or against superhydrophobic substrates. The region (i) indicates the drop region, $0 \leqslant r \leqslant \sqrt{3t}$, (ii) indicates the lamella region, $\sqrt{3t} \leqslant r \leqslant s(t)$ and (iii) the rim region. The variables $s(t)$, $b(t)$ and $v(t)$ indicate, respectively, the rim radial position, the rim thickness and the rim velocity; θ is the dynamical contact angle.

and pressures will be made non-dimensional using, as characteristic values, R, R/V and ρV^2.

The radial position and the thickness of the rim, indicated here using the time-dependent variables $s(t)$ and $b(t)$ (see figures 1 and 2), can be calculated from the following balances of mass and momentum (see appendix A)

$$\left.\begin{aligned} \alpha \frac{\pi}{4}\frac{\mathrm{d}b^2}{\mathrm{d}t} &= [u(s,t)-v]h(s,t), \qquad \frac{\mathrm{d}s}{\mathrm{d}t} = v, \\ \alpha \frac{\pi b^2}{4}\frac{\mathrm{d}v}{\mathrm{d}t} &= [u(s,t)-v]^2 h(s,t) - (1+\beta)We^{-1}, \end{aligned}\right\} \tag{2.1}$$

with $u(r,t)$ and $h(r,t)$ in (2.1) the averaged radial velocity and the thickness of the thin film – the lamella – which extends along the spatio-temporal region located in between the impacting drop and the rim, namely, $\sqrt{3t} \leqslant r \leqslant s(t)$ (see figures 1 and 2). In (2.1), we distinguish two cases depending on the wetting properties of the solid. Indeed, the sketch in figure 1 shows that the main difference existing between droplets spreading over hydrophilic or superhydrophobic substrates is that, in the latter case, the edge of the rim is never in contact with the solid. Therefore, for the case of superhydrophobic coatings, $\alpha = 1$ because the rim cross-sectional area can be approximated by that of a circle and $\beta = 1$ because the liquid in the rim is not in contact with the substrate – see figure 1 – whereas in the case of hydrophilic ones, $\alpha = 1/2$ because the rim cross-sectional area can be approximated by that of a semicircle – see figure 1 – and, since the rim contacts the solid in this case, $\beta = -\cos\theta$, with θ the advancing contact angle (Eggers *et al.* 2010).

The system of ordinary differential equations (2.1) is integrated once the averaged velocity $u(r,t)$ and the height of the liquid film $h(r,t)$ in the lamella are determined and are particularized at the radial position where the rim is located, $r = s(t)$. The differential equations for $u(r,t)$ and $h(r,t)$ are deduced in appendix A applying balances of mass and momentum to a differential portion of the lamella and taking

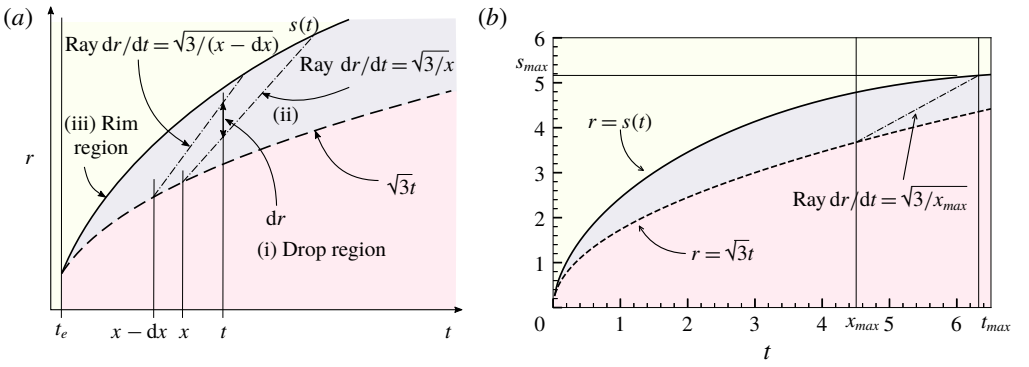

FIGURE 2. (Colour online) (*a*) Sketch showing, in a spatio-temporal diagram, the different regions defined to analyse the flow. The lamella region (ii) lies in between the end of the drop region, $r = \sqrt{3t}$ and the rim, located at $r = s(t)$. The integration of the differential equations describing the flow in the lamella is carried our along rays $\mathrm{d}r/\mathrm{d}t = u(r = \sqrt{3x}, x) = \sqrt{3/x}$ departing from the boundary $r = \sqrt{3x}$, with x a parameter denoting time. (*b*) The rays reaching the maximum radius s_{max} at the instant t_{max} depart from the boundary $r = \sqrt{3x}$ at an instant $x_{max} < t_{max}$. The curves in (*b*) have been calculated for the following values of the parameters: $Oh = 2.9 \times 10^{-3}$ and $We = 300$, which are representative values for the spreading of millimetric water droplets over a hydrophilic substrate.

into account that the lamella is a slender thin liquid film namely, $\partial h/\partial r \ll 1$, a condition which also yields that the pressure gradients in the liquid can be neglected within the spatio-temporal region $\sqrt{3t} \leqslant r \leqslant s(t)$ (see figure 2). Using these ideas, we show in appendix A that the system of partial differential equations describing the fields $u(r, t)$ and $h(r, t)$ is

$$\frac{\partial (rh)}{\partial t} + u\frac{\partial (rh)}{\partial r} = -rh\frac{\partial u}{\partial r} \quad \text{and} \quad \frac{\partial u}{\partial t} + u\frac{\partial u}{\partial r} = -\lambda \frac{u}{h\sqrt{t\,Re}}, \tag{2.2a,b}$$

with λ a free constant whose value, $\lambda = 1$, is adjusted in what follows to reproduce the experimental observations. The system (2.2) is solved specifying the values of u and h at the spatio-temporal boundary separating the drop and the lamella regions, namely, $r = \sqrt{3t}$, (see figures 1 and 2).

Notice first that, in the frictionless case $\lambda = 0$, both the height of the lamella and the liquid velocity at $r = \sqrt{3t}$ were already given using potential flow numerical simulations in Riboux & Gordillo (2016, figure 4): $u(r = \sqrt{3t}, t) = u_a(t) = \sqrt{3/t}$ and $h(r = \sqrt{3t}, t) = h_a(t)$ the function approximated by (A 20) in appendix A. For the case $\lambda \neq 0$ the presence of the boundary layer does not change, to leading order, the velocity field at surface of the drop. Therefore, the application of a mass balance in the drop region $0 \leqslant r \leqslant \sqrt{3t}$ expresses that the flow rate entering into the lamella is the same as in the potential flow case, a fact implying that, for a boundary-layer velocity profile of the type given in (A 6) in appendix A,

$$\begin{aligned} \sqrt{3/t}h_a(t) &= \sqrt{3/t}(h(r = \sqrt{3t}, t) - \delta(t)) + \sqrt{3/t}\delta(t)/2 \\ &= u(r = \sqrt{3t}, t)h(r = \sqrt{3t}, t), \end{aligned} \tag{2.3}$$

with $\delta(t)$ the thickness of the boundary layer and, hence, for $\lambda \neq 0$,

$$\left.\begin{aligned} h(r=\sqrt{3t},\, t) &= h_a(t)\left(1+\frac{\delta(t)}{2h_a(t)}\right) \\ u(r=\sqrt{3t},\, t) &= u_a(t)\left(1+\frac{\delta(t)}{2h_a(t)}\right)^{-1} \\ \text{with } u_a(t) &= \sqrt{3/t} \text{ and } \delta(t) = \sqrt{t/Re}. \end{aligned}\right\} \tag{2.4}$$

3. Solution of the equations describing flow in the lamella

The solution to the system of equations (2.1), (2.2) and (2.4) could be accomplished numerically, as is reported in Quintero *et al.* (2019), but the purpose here is to provide an approximate analytical solution in the limit $Re \gg 1$, which will be shown to be in excellent agreement with experiments, thus notably simplifying the calculations. With that idea in mind, notice first that the $Re^{-1/2}$ dependence depicted in (2.2) suggests that the fields $u(r, t)$ and $h(r, t)$ can be expressed as

$$\left.\begin{aligned} u(r,\, t) &= u_0(r,\, t) + Re^{-1/2}u_1(r,\, t) + O(Re^{-1}), \\ h(r,\, t) &= h_0(r,\, t) + Re^{-1/2}h_1(r,\, t) + O(Re^{-1}). \end{aligned}\right\} \tag{3.1}$$

Indeed, the substitution of the ansatz (3.1) into (2.2) yields the following two equations for $u_0(r, t)$ and $h_0(r, t)$:

$$\left.\begin{aligned} \frac{\partial u_0}{\partial t} + u_0\frac{\partial u_0}{\partial r} = 0 \implies \frac{\mathrm{D}u_0}{\mathrm{D}t} = 0 \\ \frac{\partial (rh_0)}{\partial t} + u_0\frac{\partial (rh_0)}{\partial r} = -rh_0\frac{\partial u_0}{\partial r} \implies \frac{\mathrm{D}(rh_0)}{\mathrm{D}t} = -rh_0\frac{\partial u_0}{\partial r}, \end{aligned}\right\} \tag{3.2}$$

with $\mathrm{D}/\mathrm{D}t \equiv \partial/\partial t + u_0\partial/\partial r$, and the following two additional equations for $u_1(r, t)$ and $h_1(r, t)$:

$$\left.\begin{aligned} \frac{\partial u_1}{\partial t} + u_0\frac{\partial u_1}{\partial r} + u_1\frac{\partial u_0}{\partial r} = -\frac{\lambda u_0}{h_0\sqrt{t}} \implies \frac{\mathrm{D}u_1}{\mathrm{D}t} + u_1\frac{\partial u_0}{\partial r} = -\frac{\lambda u_0}{h_0\sqrt{t}} \quad \text{and} \\ \frac{\partial (rh_1)}{\partial t} + u_0\frac{\partial (rh_1)}{\partial r} + u_1\frac{\partial (rh_0)}{\partial r} = -rh_0\frac{\partial u_1}{\partial r} - rh_1\frac{\partial u_0}{\partial r} \\ \implies \frac{\mathrm{D}(rh_1)}{\mathrm{D}t} + rh_1\frac{\partial u_0}{\partial r} = -\frac{\partial}{\partial r}(rh_0u_1). \end{aligned}\right\} \tag{3.3}$$

Equations (3.2) and (3.3) need to satisfy the boundary conditions deduced from (2.4) at the boundary $(r, t) = (\sqrt{3x}, x)$ separating the drop and the lamella regions. For those cases in which $\delta(x) = \sqrt{x/Re} \ll h_a(x)$ the Taylor expansion of u in (2.4) yields $u(r = \sqrt{3x}, x) \simeq u_a(x)(1 - \delta(x)/(2h_a(x)))$. It happens, however, that in spite of $Re \gg 1$, the ratio $\delta(x)/h_a(x)$ could be close to unity for sufficiently large values of the Ohnesorge number or for sufficiently large times after impact (Eggers *et al.* 2010; Visser *et al.* 2015). Motivated by this fact, the boundary conditions in (2.4) will be approximated here as

$$h(\sqrt{3x}, x) = h_a(x) + \frac{\sqrt{x}}{2}Re^{-1/2}; \quad u(\sqrt{3x}, x) \simeq \sqrt{\frac{3}{x}} - \frac{\sqrt{3}\chi}{2h_a(x)}Re^{-1/2}, \tag{3.4a,b}$$

with χ a constant such that the expression in (3.4) is a good approximation to the exact value of u in (2.4) for all values of t. Indeed, consider for instance that $\delta/h \simeq 1$: in this case, equation (3.4) would be, for $\chi = 2/3$, an excellent approximation to the initial condition for u in (2.4). For the range of Ohnesorge numbers considered here, $10^{-3} \lesssim Oh \lesssim 10^{-2}$, the ratio $\delta(t)/h_a(t)$ is close to unity or even slightly larger than one and, hence, equation (3.4) is a very good approximation to the exact value of u given in (2.4) for $\chi = 0.6$; this is the reason why all the results presented here have been calculated for $\chi = 0.6$. Notice, however, that for the impact of drops with values of the Ohnesorge number larger than those considered here, $\delta/h_a > 1$ and χ in (3.4) should be even smaller i.e. $\chi < 0.6$.

From (3.1) and (3.4) it is thus deduced that

$$\left.\begin{gathered} u_0 = \sqrt{\frac{3}{x}}, \quad u_1 = -\frac{\sqrt{3}\chi}{2h_a(x)}, \quad h_0 = h_a(x) \quad \text{and} \quad h_1 = \frac{\sqrt{x}}{2} \\ \text{at } (r, t) = (\sqrt{3x}, x). \end{gathered}\right\} \tag{3.5}$$

The integration along rays $\mathrm{d}r/\mathrm{d}t = \sqrt{3/x}$ of the momentum equation in (3.2), subjected to the corresponding boundary condition in (3.5), yields (see figure 2*a*)

$$\left.\begin{gathered} u_0(r, t) = \sqrt{\frac{3}{x}} \quad \text{along} \quad \frac{\mathrm{d}r}{\mathrm{d}t} = \sqrt{\frac{3}{x}} \Longrightarrow r = \sqrt{3x} + \sqrt{\frac{3}{x}}(t - x) \\ \Longrightarrow r = \sqrt{\frac{3}{x}}t \Longrightarrow x = 3\left(\frac{t}{r}\right)^2 \Longrightarrow u_0(r, t) = \sqrt{\frac{3}{3(t/r)^2}} = \frac{r}{t}. \end{gathered}\right\} \tag{3.6}$$

Moreover, the integration of the equation for $h_0(r, t)$ in (3.2) along the ray $\mathrm{d}r/\mathrm{d}t = \sqrt{3/x}$ yields

$$\left.\begin{gathered} \frac{\partial(rh_0)}{\partial t} + u_0\frac{\partial(rh_0)}{\partial r} + \frac{rh_0}{t} = 0 \Longrightarrow \frac{\mathrm{D}(rh_0t)}{\mathrm{D}t} = 0 \\ \Longrightarrow h_0(r, t) = 9\frac{t^2}{r^4}h_a[3(t/r)^2], \end{gathered}\right\} \tag{3.7}$$

where we have made use of the fact that $\partial u_0/\partial r = 1/t$, of the relationship between x with r and t in (3.6) and of the corresponding boundary condition in (3.5).

Now, multiplying by t both sides of equations in (3.3), one obtains that:

$$\frac{\mathrm{D}(u_1t)}{\mathrm{D}t} = -\frac{\lambda u_0}{h_0\sqrt{t}}t, \qquad \frac{\mathrm{D}(rh_1t)}{\mathrm{D}t} = -\frac{1}{t}\frac{\partial}{\partial r}(rh_0tu_1t). \tag{3.8a,b}$$

The equation for u_1 in (3.8) can be integrated along rays $r = \sqrt{3/x}t$ (see figure 2*a*) taking into account that, by virtue of (3.7), $\mathrm{D}(rh_0t)/\mathrm{D}t = 0$:

$$\left.\begin{gathered} \frac{\mathrm{D}(u_1t)}{\mathrm{D}t} = -\frac{\lambda u_0}{h_0\sqrt{t}}t \Longrightarrow \frac{\mathrm{D}(u_1t)}{\mathrm{D}t} = -\frac{\lambda u_0rt^2}{rh_0t\sqrt{t}} = -\frac{\lambda u_0}{rh_0t\sqrt{t}}\sqrt{\frac{3}{x}}t^3 \\ \Longrightarrow \frac{\mathrm{D}(u_1trh_0t)}{\mathrm{D}t} = \frac{-3\lambda}{x}t^{5/2} \\ \Longrightarrow u_1(r, t) = -\frac{1}{th_a(x)}\left[\frac{\sqrt{3}\chi x}{2} + \frac{2\sqrt{3}\lambda}{7x^{5/2}}(t^{7/2} - x^{7/2})\right], \end{gathered}\right\} \tag{3.9}$$

where we made use of the boundary condition for u_1 in (3.5) and also of the fact that, along rays $\mathrm{d}r/\mathrm{d}t = u_0 = \sqrt{3/x}$ departing from the spatio-temporal boundary $(r, t) = (\sqrt{3x}, x)$, $r = \sqrt{3/x}t$, $u_0 = \sqrt{3/x}$ and $rh_0t = \sqrt{3x}h_a(x)x$ (see figure 2*a*).

To integrate the equation for h_1 in (3.8) it is first convenient to notice that $\partial(u_1 trh_0 t)/\partial r$ can be calculated as the increment $d(u_1 trh_0 t)$ between two neighbouring rays departing from the spatio-temporal boundary $(r, t) = (\sqrt{3x}, x)$ at the consecutive instants $x - \mathrm{d}x$ and x which, at a given instant t are thus separated a distance $\mathrm{d}r = \sqrt{3}/2x^{-3/2}t\mathrm{d}x$ (see figure 2*a*). Consequently, making use of the solution for $u_1 trh_0 t$ in (3.9) and of $\mathrm{d}r = \sqrt{3}/2x^{-3/2}t\mathrm{d}x$,

$$-\frac{1}{t}\frac{\partial}{\partial r}(u_1 trh_0 t) = -\frac{2}{14\sqrt{3}t^2}[(52.5\chi - 30\lambda)x^3 - 12\lambda x^{-1/2}t^{7/2}], \tag{3.10}$$

where use of the boundary condition for u_1 in (3.5) has been made.

Hence, the integration of the equation for h_1 in (3.8) along the ray $\mathrm{d}r/\mathrm{d}t = \sqrt{3/x}$ yields

$$\left.\begin{aligned} rh_1 t - \sqrt{3x}xh_1(x) &= \frac{2}{14\sqrt{3}}\left[(52.5\chi - 30\lambda)x^3(t^{-1} - x^{-1})\right. \\ &\quad \left. + \frac{24\lambda}{5}x^{-1/2}(t^{5/2} - x^{5/2})\right] \\ \Longrightarrow h_1(r, t) &= \frac{1}{rt}\left[\frac{\sqrt{3}}{2}x^2 + \frac{\sqrt{3}(105\chi - 60\lambda)}{42}x^3(t^{-1} - x^{-1})\right. \\ &\quad \left. + \frac{24\sqrt{3}\lambda}{105}x^{-1/2}(t^{5/2} - x^{5/2})\right], \end{aligned}\right\} \tag{3.11}$$

where use of the result in (3.10) and of the boundary condition for h_1 in (3.5) has been made. Equations (3.1), (3.6), (3.7), (3.9), (3.11) provide the following expressions for $u(r, t)$ and $h(r, t)$:

$$\left.\begin{aligned} u(r, t) &= \frac{r}{t} - \frac{Re^{-1/2}}{t}\left[\frac{\sqrt{3}\chi x}{2h_a(x)} + \frac{2\sqrt{3}\lambda}{7h_a(x)x^{5/2}}(t^{7/2} - x^{7/2})\right] + O(Re^{-1}) \\ h(r, t) &= 9\frac{t^2}{r^4}h_a[3(t/r)^2] + \frac{Re^{-1/2}}{rt}\left[\frac{\sqrt{3}}{2}x^2 + \frac{\sqrt{3}(105\chi - 60\lambda)}{42}x^3(t^{-1} - x^{-1})\right. \\ &\quad \left. + \frac{24\sqrt{3}\lambda}{105}x^{-1/2}(t^{5/2} - x^{5/2})\right] + O(Re^{-1}). \end{aligned}\right\} \tag{3.12}$$

Figure 3 shows that our theoretical prediction for the height of the lamella given in (3.12) in the limit $Re \to \infty$, with $h_a(x)$ approximated by (A 20) in appendix A, is in excellent agreement with the results obtained from the boundary integral numerical simulations reported in Riboux & Gordillo (2016); the predicted values of $h(r, t)$ calculated using other theoretical approaches are also included in this figure.

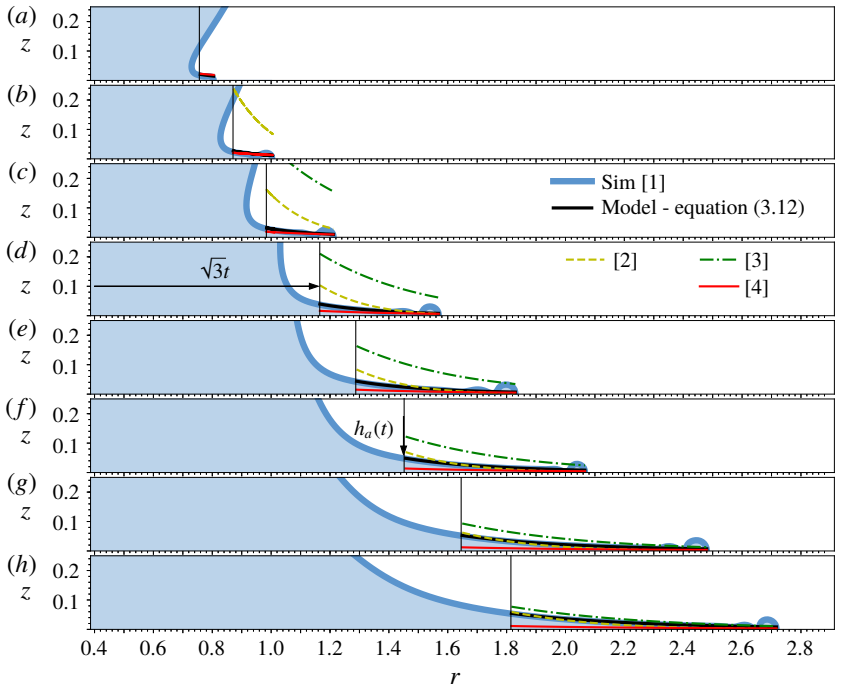

FIGURE 3. (Colour online) (*a*) The analytical expression for $h_0(r, t) = 9t^2/r^4 h_a[3(t/r)^2]$ in (3.12), represented with a black line accurately predicts, in the lamella region $\sqrt{3t} \leqslant r < s(t)$, the thickness of the thin liquid film calculated numerically in Riboux & Gordillo (2016) [1], for the free slip case ($\lambda = 0$, $Re \to \infty$) and $We = 100$: notice that the simulations in Riboux & Gordillo (2016) reveal that $h(r, t)$ does not depend on We for $We \gg 1$. (*a*) $t = 0.19$, (*b*) 0.25, (*c*) 0.32, (*d*) 0.45, (*e*) 0.55, (*f*) 0.70, (*g*) 0.90 and (*h*) $t = 1.10$. The functions $h(r, t)$ predicted using the theoretical approaches in Roisman (2009) [2], Eggers *et al.* (2010) [3], Wang & Bourouiba (2017) [4] are also included in this figure.

4. Comparison with experiments

The analytical expressions of $u(r, t)$ and $h(r, t)$ are given by (3.12), so we can now proceed to integrate the system (2.1) once the initial values for s, v and b are specified at the instant the lamella is initially ejected. Indeed, the thin liquid film is not formed right at the instant $t = 0$ when the drop first touches the substrate, but at the ejection time $t_e > 0$ determined in Riboux & Gordillo (2014, 2017). In Riboux & Gordillo (2014, 2017) we predicted and also verified experimentally that, if $Re^{1/6}Oh^{2/3} < 0.25$, a condition which is fulfilled by all experimental conditions reported here, the ejection time can be expressed as $t_e = 1.05We^{-2/3}$. Then, the system (2.1) is integrated in time once the functions $u(r, t)$ and $h(r, t)$ in (3.12) are particularized at $r = s(t)$ and once the following initial conditions are imposed at $t = t_e$ (Riboux & Gordillo 2015): $s(t_e) = \sqrt{3t_e}$, $v(t_e) = (1/2)\sqrt{3/t_e}$ and $b(t_e) = \sqrt{12}t_e^{3/2}/\pi$. The results obtained integrating the system (2.1) once the value of the free constant λ is fixed here to $\lambda = 1$, are in remarkable agreement with experimental observations for the two types of substrates considered here, as figures 4 and 5 show.

Figure 6 shows a comparison between theory and the measured values of $s(t)$ in Visser *et al.* (2015), who analysed the spreading of micrometre-sized droplets

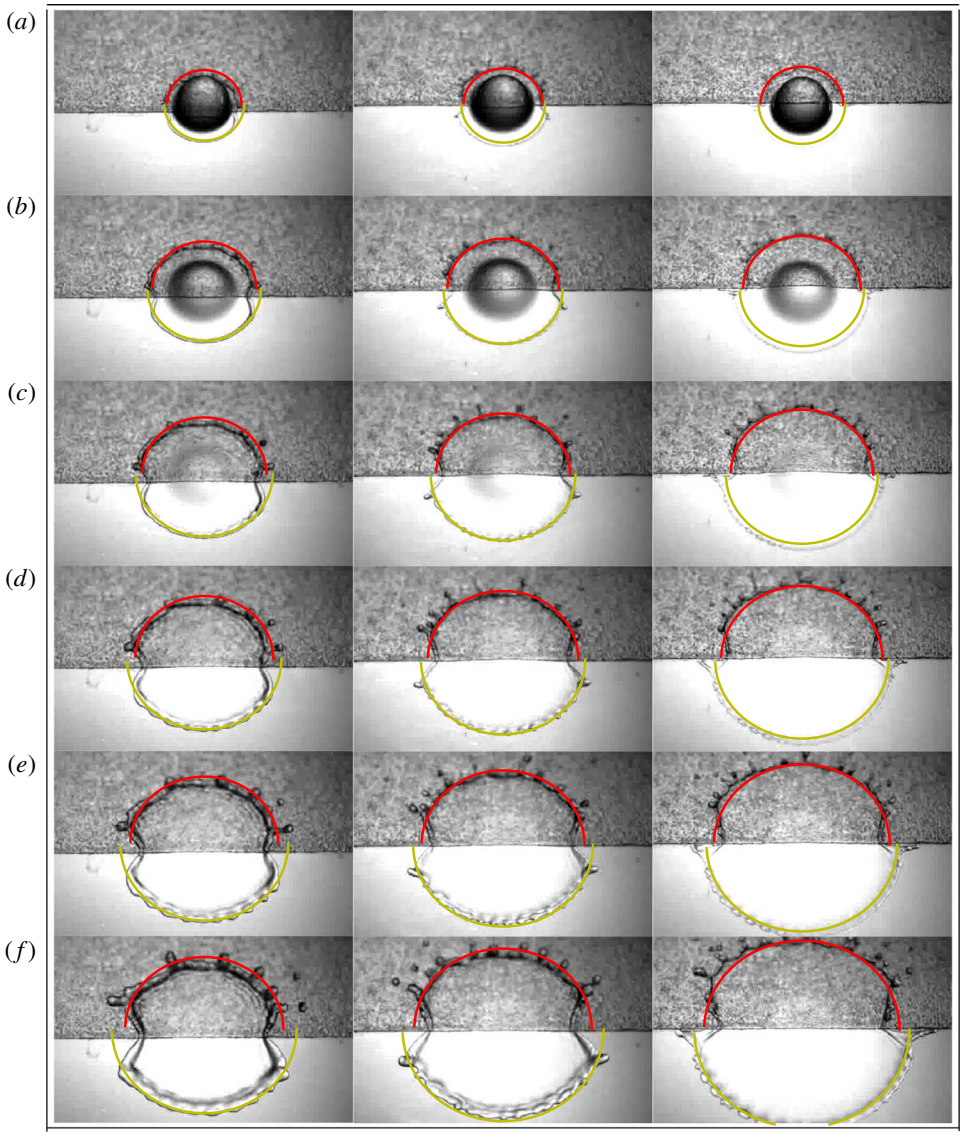

FIGURE 4. (Colour online) Comparison between the predicted and the observed position of the rim bordering the expanding lamella for the case of a water droplet of radius $R = 1.46$ mm impacting against a superhydrophobic substrate (top part of each image) or against a hydrophilic substrate (bottom part of each image). From left to right, $V = 1.59$ m s^{-1} ($We = 50$), $V = 1.94$ m s^{-1} ($We = 76$) and $V = 2.37$ m s^{-1} ($We = 114$). The values of the dimensionless instants of time corresponding to each of the rows in the figure are: (*a*) $t = T(V/R) \approx 0.5$, (*b*) $t \approx 1.0$, (*c*) 1.5, (*d*) 2.0 and (*e*) 2.5 and (*f*) 3.5.

impacting a solid substrate at velocities exceeding 10 m s^{-1}. The cases studied in Visser *et al.* (2015) correspond to values of the Ohnesorge number $Oh \sim 2 \times 10^{-2}$, an order of magnitude larger than the values of Oh in figures 4 and 5; hence, in Visser *et al.* (2015), the value of the ratio $\delta(t)/h_a(t)$ is close to unity for all t. The good

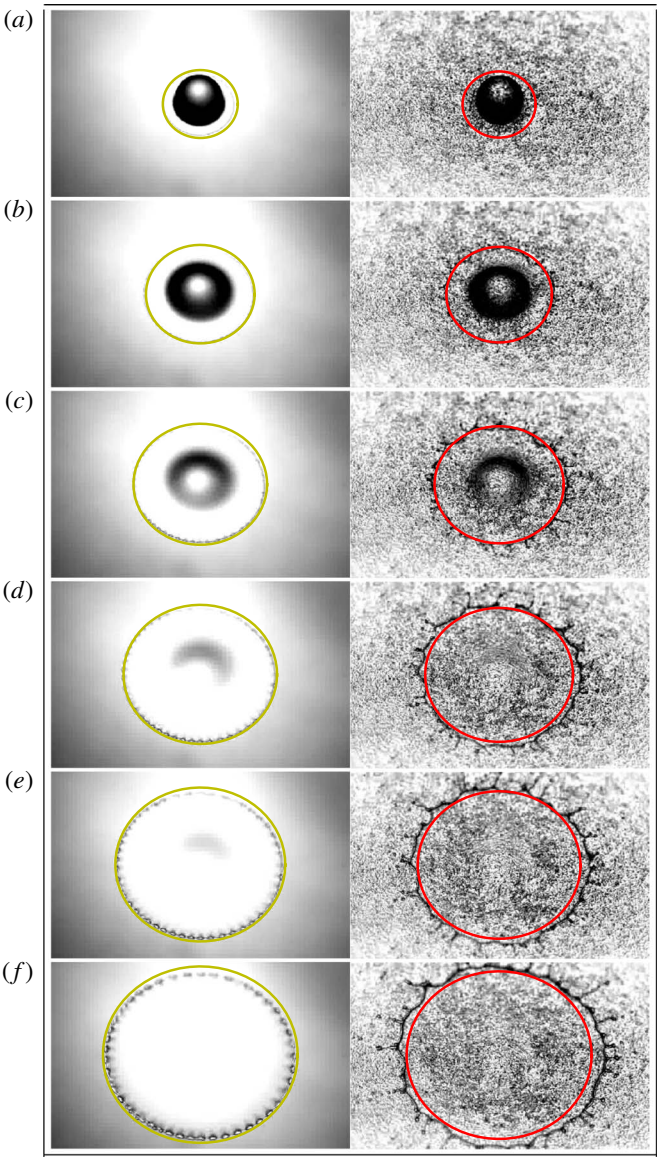

FIGURE 5. (Colour online) Comparison between the predicted and the observed position of the rim bordering the expanding lamella for the case of a water droplet of radius $R = 1.43$ mm impacting against a glass substrate (left, $V = 3.57$ m s^{-1}, $We = 261$) or a superhydrophobic substrate (right, $V = 3.58$ m s^{-1}, $We = 264$). The values of the dimensionless instants of time corresponding to each of the rows in the figure are: (*a*) $t = T(V/R) \approx 0.5$, (*b*) $t \approx 1.0$, (*c*) 1.5, (*d*) 2.0 and (*e*) 2.5 and (*f*) 3.5.

agreement between the theoretical and experimental results depicted in figure 6, gives strong further support to our theory.

The integration of the system (2.1) could be avoided if just the maximum spreading radius of the drop, s_{max}, had to be predicted. Indeed, figure 7 indicates states that, very

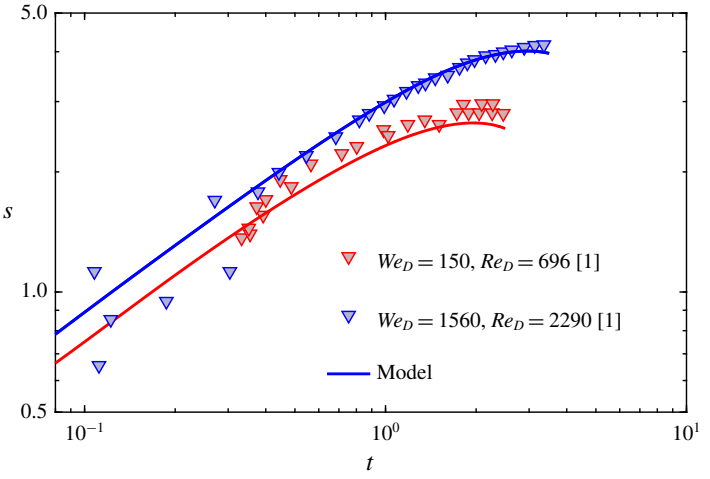

FIGURE 6. (Colour online) Comparison between the experimental data in Visser *et al.* (2015) [1] and the theoretical results. Here, $\beta = 1$ and, as in the rest of calculations presented here, $\lambda = 1$ and $\chi = 0.6$. $We_D = 2We$ and $Re_D = 2Re$ because Visser *et al.* (2015) defined the Weber and Reynolds numbers using the diameter instead of the drop radius.

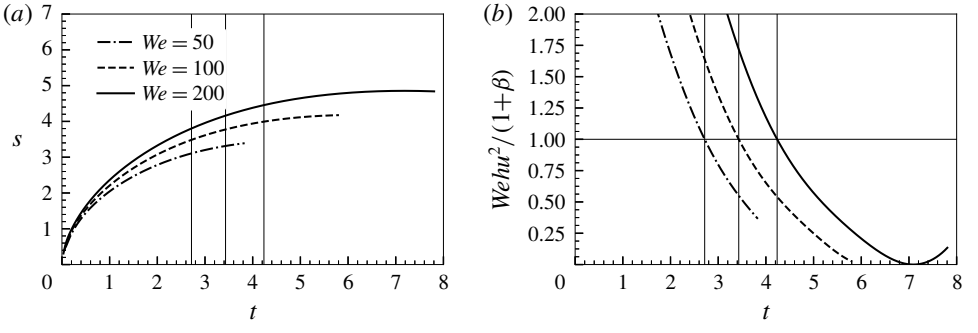

FIGURE 7. (*a*) Calculated position of the rim for $Oh = 2.9 \times 10^{-3}$ and three values of the Weber number. The vertical lines indicate the instant of time for which the value of the local Weber number defined in (4.1) is equal to one. (*b*) Time evolution of the local Weber number defined in (4.1).

close to the maximum spreading radius, the rim velocity is zero and also that the value of the local Weber number, defined here as

$$We_{local}(t) = We\frac{u^2(s,t)h(s,t)}{1+\beta}, \tag{4.1}$$

is $We_{local} \simeq 1$. Therefore, the substitution into the momentum equation in (2.1) of $v = 0$, of $\mathrm{d}v/\mathrm{d}t = 0$ and of the values of the functions $u(r, t)$ and $h(r, t)$ given in (3.12) particularized at $r = s_{max}$ and at $t = t_{max}$, with t_{max} the instant of time at which

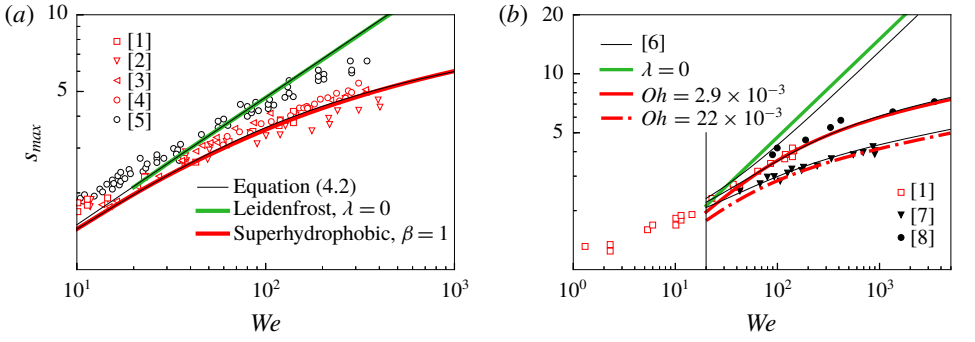

FIGURE 8. (Colour online) (*a*) Comparison between the experimental data in [1] Clanet *et al.* (2004), [2] Tsai *et al.* (2011), [3] Antonini *et al.* (2012), [4] Quintero *et al.* (2019), [5] Tran *et al.* (2012) and the maximum spreading radius calculated solving the algebraic equation (4.3) – continuous lines. (*b*) Comparison between the experimental data and theory in [6] Wildeman *et al.* (2016) (thin black lines), [7] Stow, Hadfield & Ziman (1981) and [8] Visser *et al.* (2015) and the maximum spreading radius calculated theoretically solving the algebraic equation (4.3) – thick lines. The results have been obtained for the same values of β as in [6] Wildeman *et al.* (2016), $\beta = 1$.

$r = s_{max}$ yields, to leading order, in the limits $We \gg 1$ and $Re \gg 1$, the following equation for s_{max}:

$$\left.\begin{aligned} & h_0 u_0^2 + Re^{-1/2}(h_1 u_0^2 + 2h_0 u_0 u_1) - (1+\beta)We^{-1} = 0 \\ \Longrightarrow\ & 9h_a(x_{max}) - 3^{3/4}\frac{12\lambda x_{max}^{-3/4}}{35} Re^{-1/2} s_{max}^{5/2} - (1+\beta)We^{-1} s_{max}^2 = 0, \end{aligned}\right\} \tag{4.2}$$

with $x_{max} = 3(t_{max}/s_{max})^2$ and where $O(Re^{-1})$ terms have been neglected. Moreover, in spite of the value of x_{max} depends on We, Re and θ, we checked that x_{max} lies within a limited range of values, such that $t_{max} > x_{max}$, see figure 2(*b*).

Therefore, we could further simplify (4.2) if x_{max} is approximated by a constant value which we fix here to $x_{max} = 2$, for which $9h_a(x_{max}) \simeq 0.45$ (see (A 20) in appendix A) and $3^{3/4}(12x_{max}^{-3/4})/35 \simeq 0.45$. Therefore, equation (4.2) can be written as

$$(1+\beta)We^{-1} s_{max}^2 + 0.45\lambda Re^{-1/2} s_{max}^{5/2} - 0.45 = 0, \tag{4.3}$$

which resembles the equation for s_{max} deduced in Wildeman *et al.* (2016) using energetic arguments. Let us point out here that (4.2) and (4.3) express the same type of balance as that found in the study of Savart sheets: the momentum flux is compensated with the interfacial tension forces at the maximum spreading radius (Taylor 1959; Gordillo, Lhuissier & Villermaux 2014).

Figures 8(*a*,*b*) shows that our prediction for s_{max} calculated using (4.3) compares very favourably with published experimental data, providing further support to our theoretical approach. Another evidence showing the robustness of our analysis is given next. Indeed, a direct comparison of our theoretical result in (4.3) with the equation for the maximum spreading radius in Laan *et al.* (2014) – which in our variables can be written as

$$s_{max}^{Laan} = Re^{1/5} 2^{1/5} \frac{P^{1/2}}{1+P^{1/2}} = Re^{1/5} \bar{f}(P) \tag{4.4}$$

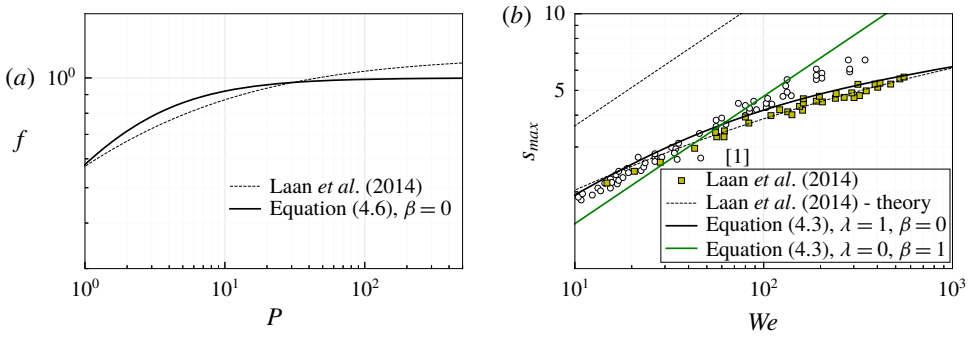

FIGURE 9. (Colour online) (*a*) Comparison between the Padè approximant in Laan *et al.* (2014) and the function $f(P)$ predicted by our theoretical result in (4.6). (*b*) s_{max} calculated using (4.3) and the equation in Laan *et al.* (2014), $s_{max} = 2^{1/5} We^{1/2}$ for the case of Leidenfrost droplets, $\lambda = 0$.

with $P = We\, Re^{-2/5}$ – can be easily made once we express s_{max} as

$$s_{max} = Re^{1/5} f. \tag{4.5}$$

The substitution of (4.5) into (4.3) yields the following expression for $f(P)$:

$$(1+\beta)P^{-1}f^2 + 0.45\lambda f^{5/2} - 0.45 = 0. \tag{4.6}$$

Figure 9, where the functions $\bar{f}(P)$ and $f(P)$ defined respectively in (4.4) and (4.6) are compared, shows that our theoretical result for $f(P)$ calculated solving equation (4.6) is very close to the Padè approximant given in Laan *et al.* (2014). However, figure 9 also shows that s_{max} calculated using (4.3) is in better agreement with experiments than the prediction in Laan *et al.* (2014) for the case of Leidenfrost droplets, $\lambda = 0$ (Tran *et al.* 2012; Wildeman *et al.* 2016).

5. Conclusions

In this contribution we have presented a model which is not only able to predict, in a self-consistent way, the maximum spreading diameter of drops impacting a solid wall, but also the time evolution of the position and of the thickness of the rim. Our theory also provides the averaged velocity field and the thickness of the thin film region located upstream the rim for arbitrary values of the advancing contact angle and of the Reynolds and Weber numbers whenever $Re \gg 1$ and $We \gg 1$. The good agreement of our predictions with the experimental observations indicates that our results could also be used to determine the time evolution of the diameters and of the sizes of the droplets ejected for drop impact velocities beyond the splashing threshold (Riboux & Gordillo 2015; Quintero *et al.* 2019).

Acknowledgements

This study has been financially supported by the Spanish MINECO under Projects DPI2014-59292-C3-2-P, DPI2017-88201-C3-1-R and DPI2015-71901-REDT, and partly financed through European funds.

Appendix A

The radial position and the thickness of the rim, indicated here using the time-dependent variables $s(t)$ and $b(t)$ (see figures 1 and 2), can be calculated from the following balances of mass and momentum at the rim (Taylor 1959; Culick 1960)

$$\left.\begin{aligned} \alpha\frac{\pi}{4}\frac{\mathrm{d}b^2}{\mathrm{d}t} &= \int_0^{h(s,t)} \bar{u}(s,z,t)\,\mathrm{d}z - vh(s,t), \quad \frac{\mathrm{d}s}{\mathrm{d}t} = v, \\ \alpha\frac{\pi b^2}{4}\frac{\mathrm{d}v}{\mathrm{d}t} &= \int_0^{h(s,t)} [\bar{u}(s,z,t)-v]^2\,\mathrm{d}z - (1+\beta)We^{-1} - f_\tau, \end{aligned}\right\} \tag{A 1}$$

with z the coordinate perpendicular to the wall, f_τ the viscous friction at the wall and $\bar{u}(r,z,t)$ and $h(r,t)$ in (A 1) the radial velocity and the thickness of the thin film – the lamella – which extends along the spatio-temporal region located in between the impacting drop and the rim, namely, $\sqrt{3t} \leqslant r \leqslant s(t)$ (see figures 1 and 2). We will show next that, to solve the system of (A 1), it will suffice to know the values of the height of the lamella particularized at $r = s(t)$ and also the averaged value of the radial velocity at $r = s(t)$. Indeed, notice first that, for a given velocity field $\bar{u}(r,z,t)$, the mass balance applied to a portion of the lamella of height $h(r,t)$, width $\mathrm{d}r$ and angular extension $\mathrm{d}\eta$ yields

$$\frac{\partial(rh)}{\partial t} + \frac{\partial}{\partial r}\left(r\int_0^h \bar{u}(r,z,t)\,\mathrm{d}z\right) = 0. \tag{A 2}$$

Defining the averaged velocity $u(r,t)$ as

$$u(r,t)h(r,t) = \int_0^h \bar{u}(r,z,t)\,\mathrm{d}z, \tag{A 3}$$

the mass balance (A 2) reads

$$\frac{\partial(rh)}{\partial t} + \frac{\partial}{\partial r}(ruh) = 0. \tag{A 4}$$

The application of the momentum balance to the same differential portion of the lamella yields

$$\frac{\partial}{\partial t}(ruh) + \frac{\partial}{\partial r}\left(r\int_0^h \bar{u}^2(r,z,t)\,\mathrm{d}z\right) = -\frac{r\tau_w}{Re}, \tag{A 5}$$

where we have taken into account that the lamella is slender and, hence, pressure gradients can be neglected; in (A 5) τ_w indicates the dimensionless shear stress at the wall. Since the integral form of the momentum equation (A 5) is not strongly dependent on the specific form of the boundary-layer type of velocity profile (see the discussion in (Batchelor 1967, pp. 319–320) about the integral method to analyse boundary layers firstly introduced by von Kármán), for simplicity we assume here that

$$\begin{aligned} \bar{u}(r,z,t) = w_0(r,t) - w_0F(z) \quad &\text{with } F(z) = 1 - z/\delta \text{ for } z \leqslant \delta \\ &\text{and } F(z) = 0 \quad \text{if } z > \delta, \end{aligned} \tag{A 6a,b}$$

with δ the boundary-layer thickness. Making use of (A 6) and of the fact that

$$\int_0^h F(z)\,\mathrm{d}z = \delta/2 \quad \text{and} \quad \int_0^h F^2(z)\,\mathrm{d}z = \delta/3, \tag{A 7a,b}$$

equation (A 3) yields

$$u(r,t)h(r,t) = \int_0^h \bar{u}(r,z,t)\,\mathrm{d}z = w_0(r,t)h(r,t)(1-\delta/(2h)) \Rightarrow w_0 = \frac{u}{1-\delta/(2h)}. \tag{A 8}$$

Therefore, using (A 6) and (A 8), the momentum flux can be expressed as

$$\int_0^h \bar{u}\bar{u}\,\mathrm{d}z = u^2 h + \frac{u^2 h}{(1-\delta/(2h))^2}\left[\frac{\delta}{3h} - \left(\frac{\delta}{2h}\right)^2\right] \tag{A 9}$$

and, consequently, equation (A 5) can be written as

$$\frac{\partial}{\partial t}(ruh) + \frac{\partial}{\partial r}(ru^2 h) = -\frac{r\tau_w}{Re} - \frac{\partial}{\partial r}\left(\frac{ru^2 h}{(1-\delta/(2h))^2}\left[\frac{\delta}{3h} - \left(\frac{\delta}{2h}\right)^2\right]\right). \tag{A 10}$$

Using (A 6) and (A 8), the dimensionless shear stress at the wall can be expressed as

$$\tau_w = \frac{w_0}{\delta} = \frac{u}{\delta(1-\delta/(2h))} \tag{A 11}$$

and hence, making use of the continuity (A 4), the momentum equation (A 10) can be written as

$$\frac{\partial u}{\partial t} + u\frac{\partial u}{\partial r} = -\frac{u}{hRe\delta(1-\delta/(2h))} - \frac{1}{rh}\frac{\partial}{\partial r}\left(\frac{ru^2 h}{(1-\delta/(2h))^2}\left[\frac{\delta}{3h} - \left(\frac{\delta}{2h}\right)^2\right]\right). \tag{A 12}$$

Let us point out that in the limit $\delta/h \ll 1$ the boundary-layer thickness does not depend on r but, interestingly, there are two different algebraic expressions for $\delta(t)$. Indeed, for $t \approx t_e \ll 1$, with $t_e \propto We^{-2/3}$ the instant of time at which the liquid sheet is first ejected, the lamella is fed by the fluid coming from a local region surrounding the root of the lamella; in this case, $\delta(t) \propto tRe^{-1/2}$ (Riboux & Gordillo 2014, 2015, 2017). However, for larger times, the fluid entering the liquid sheet comes from a stagnation-point type of flow and, in this case, $\delta \propto \sqrt{t}Re^{-1/2}$ (Roisman 2009; Eggers *et al.* 2010). Since the time interval during which $\delta \propto tRe^{-1/2}$ is $t \sim t_e \ll 1$ namely, much smaller than the time characterizing the drop spreading process, the equation for $\delta(t)$ used here is $\delta = \sqrt{t/Re}$ (Roisman 2009; Eggers *et al.* 2010). Therefore, since the lamella is slender, $\partial h/\partial r \ll 1$, equation (A 12) can be written as

$$\frac{\partial u}{\partial t} + u\frac{\partial u}{\partial r} = -\frac{u}{hRe\delta}\left[\frac{1}{1-\delta/(2h)} + \frac{1}{(1-\delta/(2h))^2}\left(\frac{1}{3} - \frac{1}{4}\frac{\delta}{h}\right)\left(\frac{ut}{r} + 2t\frac{\partial u}{\partial r}\right)\right]. \tag{A 13}$$

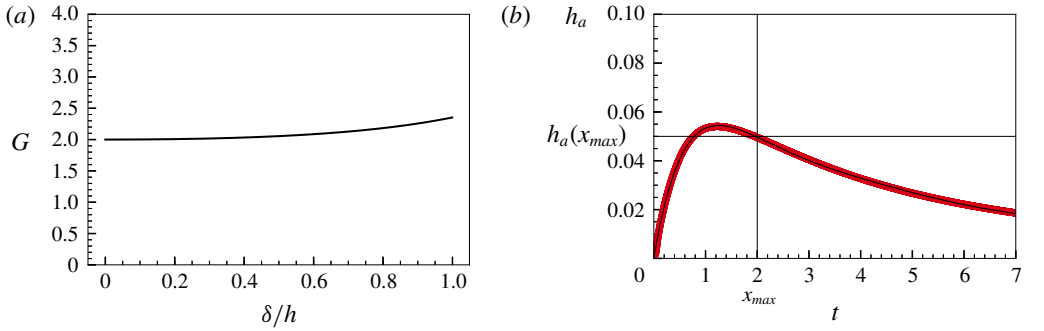

FIGURE 10. (Colour online) (*a*) Representation of the function G defined in (A 14) as a function of the ratio δ/h. (*b*) The polynomial $P(x)$ in (A 20) (black line) matches the time evolution of the height of the lamella calculated at $r=\sqrt{3x}$ using the boundary integral method described in Riboux & Gordillo (2016). The function $h_a(x)$ does not depend neither on Re nor on We for $We \gg 1$. Here, $We = 300$.

In the frictionless case, $u = r/t$ (Roisman 2009; Eggers *et al.* 2010) and hence, the right-hand side of (A 13) verifies, for $\delta = \sqrt{t/Re}$

$$\frac{1}{1-\delta/(2h)} + \frac{1}{(1-\delta/(2h))^2}\left(\frac{1}{3} - \frac{1}{4}\frac{\delta}{h}\right)\left(\frac{ut}{r} + 2t\frac{\partial u}{\partial r}\right) \simeq G(\delta/h)$$
$$= \frac{1}{1-\delta/(2h)} + \frac{1}{(1-\delta/(2h))^2}\left(1 - \frac{3}{4}\frac{\delta}{h}\right) \simeq 2, \tag{A 14}$$

where the function $G(\delta/h)$ defined in (A 14) and plotted in figure 10(*a*), is rather insensitive to the ratio δ/h. Therefore, the momentum equation (A 12) can be written as

$$\frac{\partial u}{\partial t} + u\frac{\partial u}{\partial r} = -\frac{\lambda u}{hRe\delta} = -\frac{\lambda u}{h\sqrt{Re\, t}}, \tag{A 15}$$

with λ a constant that will take into account: (i) the prefactor multiplying the ratio $\sqrt{t/Re}$, (ii) the type of velocity profile used to describe the flow field within the boundary layer and (iii) the deviations from the assumption made here that $\delta = \sqrt{t/Re}$, a result which is only valid in the boundary-layer approach for a flow field outside the boundary layer of the form $u = r/t$ (Roisman 2009; Eggers *et al.* 2010). It will be shown in the main text the experimental results can be reproduced for a value of the constant $\lambda = 1$.

The solution of the system of partial differential equations describing both the height of the lamella $h(r, t)$ and the averaged velocity $u(r, t)$, given by (A 4) and (A 15),

$$\frac{\partial (rh)}{\partial t} + u\frac{\partial (rh)}{\partial r} = -rh\frac{\partial u}{\partial r} \quad \text{and} \quad \frac{\partial u}{\partial t} + u\frac{\partial u}{\partial r} = -\lambda\frac{u}{h\sqrt{Re\, t}}, \tag{A 16a,b}$$

particularized at $r = s(t)$, permit us to integrate the system (A 1) in time.

Indeed, notice that (A 9) can be accurately approximated as

$$\int_0^h \bar{u}\bar{u}\, \mathrm{d}z = u^2 h + \frac{u^2 h}{(1-\delta/(2h))^2}\frac{\delta}{3h}, \tag{A 17}$$

and also that the force exerted by the wall on the rim, f_τ (see (A 1)) is given by

$$f_\tau = \frac{w_0^2\delta}{3} + \gamma\, We^{-1}\, Ca\, v = \frac{u^2 h}{(1-\delta/(2h))^2}\frac{\delta}{3h} + \gamma\, We^{-1}\, Ca\, v, \tag{A 18}$$

with $\gamma \sim O(1)$. Indeed, the flux of momentum entering into the drop through the boundary layer, $w_0^2\delta/3$, does not contribute to accelerate the rim because the fraction of the momentum injected closer to the solid is decelerated by the wall. The second term at the right of (A 18) is the integral of the viscous shear forces at the wall $\sim Re^{-1}v/b$ along a region of width $\sim b$. Then, taking into account the definition of the mean velocity in (A 3), the system of (A 1) can be written as

$$\left.\begin{aligned} \alpha\frac{\pi}{4}\frac{\mathrm{d}b^2}{\mathrm{d}t} &= [u(s,t)-v]h(s,t), \qquad \frac{\mathrm{d}s}{\mathrm{d}t} = v, \\ \alpha\frac{\pi b^2}{4}\frac{\mathrm{d}v}{\mathrm{d}t} &= [u(s,t)-v]^2 h(s,t) - (1+\beta)\, We^{-1} - \gamma\, We^{-1}\, Ca\, v. \end{aligned}\right\} \tag{A 19}$$

We will limit ourselves here to discussing the cases for which $Ca \ll 1$ and hence, the last term in (A 19), will be neglected.

Let us finally point out that, in the potential flow case, the thickness of the liquid film at the boundary separating the drop and lamella regions i.e. at $r = \sqrt{3x}$, can be accurately calculated as $h_a(x) = P(x)$, with

$$\begin{aligned} P(x) \;=\; \sum_{i=0}^{9} p_i x^i \quad \text{with} \\ p_0 = 3.95812707\times10^{-4}, \quad & p_1 = 1.22669850\times10^{-1}, \\ p_2 = -1.04054024\times10^{-1}, \quad & p_3 = 4.37229580\times10^{-2}, \\ p_4 = -1.09184802\times10^{-2}, \quad & p_5 = 1.70579418\times10^{-3}, \\ p_6 = -1.67926979\times10^{-4}, \quad & p_7 = 1.01063551\times10^{-5}, \\ p_8 = -3.39290090\times10^{-7}, \quad & p_9 = 4.86535897\times10^{-9}, \end{aligned} \tag{A 20}$$

see figure 10(*b*).

REFERENCES

ANTONINI, C., AMIRFAZLI, A. & MARENGO, M. 2012 Drop impact and wettability: from hydrophilic to superhydrophobic surfaces. *Phys. Fluids* **24** (10), 102104.

BATCHELOR, G. K. 1967 *An Introduction to Fluid Dynamics*. Cambridge University Press.

CLANET, C., BÉGUIN, C., RICHARD, D. & QUÉRÉ, D. 2004 Maximal deformation of an impacting drop. *J. Fluid Mech.* **517**, 199–208.

CULICK, F. E. C. 1960 Comments on a ruptured soap film. *J. Appl. Phys.* **31**, 1128–1129.

EGGERS, J., FONTELOS, M. A., JOSSERAND, C. & ZALESKI, S. 2010 Drop dynamics after impact on a solid wall: theory and simulations. *Phys. Fluids* **22**, 062101.

GORDILLO, J. M., LHUISSIER, H. & VILLERMAUX, E. 2014 On the cusps bordering liquid sheets. *J. Fluid Mech.* **754**, R1.

JOSSERAND, C. & THORODDSEN, S. T. 2016 Drop impact on a solid surface. *Annu. Rev. Fluid Mech.* **48** (1), 365–391.

LAAN, N., DE BRUIN, K. G., BARTOLO, D., JOSSERAND, C. & BONN, D. 2014 Maximum diameter of impacting liquid droplets. *Phys. Rev. Appl.* **2**, 044018.

LAAN, N., DE BRUIN, K. G., SLENTER, D., WILHELM, J., JERMY, M. & BONN, D. 2015 Bloodstain pattern analysis: implementation of a fluid dynamic model for position determination of victims. *Sci. Rep.* **5**, 11461.

LEE, J. B., LAAN, N., DE BRUIN, K. G., SKANTZARIS, G., SHAHIDZADEH, N., DEROME, D., CARMELIET, J. & BONN, D. 2016 Universal rescaling of drop impact on smooth and rough surfaces. *J. Fluid Mech.* **786**, R4.

LEJEUNE, S., GILET, T. & BOUROUIBA, L. 2018 Edge effect: liquid sheet and droplets formed by drop impact close to an edge. *Phys. Rev. Fluids* **3**, 083601.

LV, C., HAO, P., ZHANG, X. & HE, F. 2016 Drop impact upon superhydrophobic surfaces with regular and hierarchical roughness. *Appl. Phys. Lett.* **108**, 141602.

QUINTERO, E. S., RIBOUX, G. & GORDILLO, J. M. 2019 Splashing of droplets impacting superhydrophobic substrates. *J. Fluid Mech.* (submitted).

RIBOUX, G. & GORDILLO, J. M. 2014 Experiments of drops impacting a smooth solid surface: a model of the critical impact speed for drop splashing. *Phys. Rev. Lett.* **113**, 024507.

RIBOUX, G. & GORDILLO, J. M. 2015 The diameters and velocities of the droplets ejected after splashing. *J. Fluid Mech.* **772**, 630–648.

RIBOUX, G. & GORDILLO, J. M. 2016 Maximum drop radius and critical Weber number for splashing in the dynamical Leidenfrost regime. *J. Fluid Mech.* **803**, 516–527.

RIBOUX, G. & GORDILLO, J. M. 2017 Boundary–layer effects in droplet splashing. *Phys. Rev.* E **96**, 013105.

ROISMAN, I. V. 2009 Inertia dominated drop collisions. II. An analytical solution of the Navier–Stokes equations for a spreading viscous film. *Phys. Fluids* **21**, 052104.

ROISMAN, I. V., RIOBOO, R. & TROPEA, C. 2002 Normal impact of a liquid drop on a dry surface: model for spreading and receding. *Proc. R. Soc. Lond.* A **458** (2022), 1411–1430.

STOW, C. D., HADFIELD, M. G. & ZIMAN, J. M. 1981 An experimental investigation of fluid flow resulting from the impact of a water drop with an unyielding dry surface. *Proc. R. Soc. Lond.* A **373** (1755), 419–441.

TAYLOR, G. I. 1959 The dynamics of thin sheets of fluid. III. Desintegration of fluid sheets. *Proc. R. Soc. Lond.* A **253**, 1274.

TRAN, T., STAAT, H. J. J., PROSPERETTI, A., SUN, C. & LOHSE, D. 2012 Drop impact on superheated surfaces. *Phys. Rev. Lett.* **108**, 036101.

TSAI, P., HENDRIX, M. H. W., DIJKSTRA, R. R. M., SHUI, L. & LOHSE, D. 2011 Microscopic structure influencing macroscopic splash at high Weber number. *Soft Matt.* **7**, 11325–11333.

VILLERMAUX, E. & BOSSA, B. 2011 Drop fragmentation on impact. *J. Fluid Mech.* **668**, 412–435.

VISSER, C. W., FROMMHOLD, P. E., WILDEMAN, S., METTIN, R., LOHSE, D. & SUN, C. 2015 Dynamics of high-speed micro-drop impact: numerical simulations and experiments at frame-to-frame times below 100 ns. *Soft Matt.* **11**, 1708–1722.

WANG, Y. & BOUROUIBA, L. 2017 Drop impact on small surfaces: thickness and velocity profiles of the expanding sheet in the air. *J. Fluid Mech.* **814**, 510–534.

WANG, Y., DANDEKAR, R., BUSTOS, N., POULAIN, S. & BOUROUIBA, L. 2018 Universal rim thickness in unsteady sheet fragmentation. *Phys. Rev. Lett.* **120**, 204503.

WILDEMAN, S., VISSER, C. W., SUN, C. & LOHSE, D. 2016 On the spreading of impacting drops. *J. Fluid Mech.* **805**, 636–655.